

Journal of Biomedical Optics

SPIEDigitalLibrary.org/jbo

Holographic tissue dynamics spectroscopy

David D. Nolte

Ran An

John Turek

Kwan Jeong



SPIE

Holographic tissue dynamics spectroscopy

David D. Nolte,^a Ran An,^a John Turek,^b and Kwan Jeong^c

^aPurdue University, Department of Physics, West Lafayette, Indiana 47907

^bPurdue University, Department of Basic Medical Sciences, West Lafayette, Indiana 47907

^cKorea Military Institute, Department of Physics, Seoul, Republic of Korea

Abstract. Tissue dynamics spectroscopy uses digital holography as a coherence gate to extract depth-resolved quasi-elastic dynamic light scattering from inside multicellular tumor spheroids. The temporal speckle contrast provides endogenous dynamical images of proliferating and hypoxic or necrotic tissues. Fluctuation spectroscopy similar to diffusing wave spectroscopy is performed on the dynamic speckle to generate tissue-response spectrograms that track time-resolved changes in intracellular motility in response to environmental perturbations. The spectrograms consist of several frequency bands that range from 0.005 to 5 Hz. The fluctuation spectral density and temporal autocorrelations show the signature of constrained anomalous diffusion, but with large fluctuation amplitudes caused by active processes far from equilibrium. Differences in the tissue-response spectrograms between the proliferating outer shell and the hypoxic inner core differentiate normal from starved conditions. The differential spectrograms provide an initial library of tissue-response signatures to environmental conditions of temperature, osmolarity, pH, and serum growth factors. © 2011 Society of Photo-Optical Instrumentation Engineers (SPIE). [DOI: 10.1117/1.3615970]

Keywords: dynamic light scattering; speckle imaging; membrane fluctuations; label-free; digital holography; apoptosis; tumor spheroid; coherence domain.

Paper 11012RR received Jan. 7, 2011; revised manuscript received Jun. 10, 2011; accepted for publication Jun. 13, 2011; published online Aug. 31, 2011.

1 Introduction: Coherence-Gated Tissue Dynamics

Cellular tissue is heterogeneous on all length¹ and time² scales. The dynamic character of living tissue arises from the active functions of the cytoskeleton^{3,4} and molecular motors⁵ that drive transport⁶ through the crowded cytosol⁷ in cells. As elastomechanical systems,^{8,9} the dynamics are energetically driven far from thermal equilibrium^{10,11} producing dramatic fluctuations in scattered light.

Light scattering from tissue is an important probe of cellular structure and dynamics,¹² but the challenge has been to extract high content and context information from scattered light that can compete with fluorescence techniques. This has been partially achieved using light scattering spectroscopy that detects Mie signatures in light scattered from epithelial layers^{13,14} that enables the sizing of organelles¹⁵ as a diagnostic to monitor precancerous transformations.¹⁶ Low-coherence enhanced backscatter probes subtle structural changes in tissue layers that also have an important diagnostic potential.¹⁷

Light scattered from a selected depth can be localized by applying a coherence gate on the scattered light¹⁸ as in optical coherence tomography.¹⁹ Full-field coherence gating was demonstrated using dynamic holography^{20,21} to capture depth-gated speckle fields and was applied to multicellular tumor spheroids²² and the mouse eye.²³ In the single-scattering regime, digital holography²⁴ has been applied with numerical focusing to study the refractive index profiles of cells²⁵ and in the multiple-scattering regime as a coherence gate to study the structure of tumors and the effect of anti-mitotic drugs on tissue.²⁶

Dynamic light scattering (DLS) in tissues is performed as quasi-elastic light scattering (QELS) when light is predominantly singly-scattered, and as diffusing-wave spectroscopy^{27,28} (DWS) or diffusing correlation spectroscopy²⁹ (DCS) when light is multiply scattered. QELS has been mainly applied to single cells or monolayer cultures to study motion in the nucleus,³⁰ the cytosol,³¹ cell motion,³² and membrane fluctuations.³³ DWS and DCS probe deeply into tissue and have been used to study actin filament networks,³⁴ imaging dynamic heterogeneities,³⁵ and brain activity.³⁶ Imaging approaches have been applied for speckle contrast imaging to monitor blood flow.³⁷ The transition from single-scattering to multiple scattering is important for backscatter applications,^{38,39} such as in the work presented in this paper.

Coherence-gating can be applied to dynamic light scattering to provide three-dimensional detection of the intracellular motions of cells.⁴⁰ This is the principle of motility contrast imaging (MCI), which has been applied to living tissue and used to study the effects of anti-mitotic cytoskeletal drugs on the tissue dynamics.²⁶ Coherence-gated dynamic light scattering lies between the regimes of single and multiple scattering. The coherence gate preferentially selects singly-scattered ballistic photons,^{38,39,41} but multiply scattered photons may also be path-matched to the reference beam.^{42,43}

Multiply-scattered speckle tends to be spatially uncorrelated, but exhibits a full temporal spectrum across several orders of magnitude.⁴⁴ The full spectrum is a consequence of many different internal scattering processes combined with multiple scattering of light. Dynamic processes such as cell movement, membrane distortion, undulations, and organelle transport have characteristic time scales that are mixed as light scatters many times from the multiple processes. The resulting fluctuation

Address all correspondence to: David Nolte, Purdue University, Physics, 525 Northwestern Avenue, Lafayette, Indiana 47907; Tel: 765-494-3013; E-mail: nolte@physics.psu.edu.

power spectrum rarely shows distinct spectral features because of the mixing of scattering rates. This time-scale mixing presents a severe challenge to isolate the different dynamic cellular mechanisms in the fluctuation power spectra. However, it is possible to apply specific interventions, such as environmental perturbations or drugs, and measure the differential changes in the fluctuation power spectra. These differential spectra can be specific to changes in internal functions and may provide specific signatures of drug action for drug screening applications.

In this paper, we apply coherence-gated holographic speckle fluctuation spectroscopy to study the effect of environmental perturbations on multicellular tumor spheroids. The principles of motility contrast imaging and tissue dynamics spectroscopy are described in Sec. 2, including the properties of multicellular tumor spheroids, the analysis for the temporal autocorrelations (that shows the signature of constrained motion), and the analysis for the differential spectrograms. The importance of tissue preconditions and stability are presented in Sec. 3, followed by perturbations to the tissue in Sec. 4 that include serum in the growth medium, temperature, osmolarity, and pH.

2 Motility Contrast Imaging and Tissue Dynamics Spectroscopy

The holographic capture of depth-resolved images from optically thick living tissues has evolved through several stages. Optical coherence imaging (OCI) uses coherence-gated holography to optically section tissue up to 1 mm deep.^{20,45} It is a full-frame imaging approach, closely related to *en face* optical coherence tomography,^{46,47} but with deeper penetration and high-contrast speckle because of the simultaneous illumination of a broad area.⁴⁸ The first implementations of OCI used dynamic holographic media⁴⁹ such as photorefractive quantum wells⁵⁰ to capture the coherent backscatter and separate it from the high diffuse background. Digital holography^{51–54} approaches replaced the dynamic media and have become the mainstay of current implementations of OCI.⁵⁵ Highly dynamic speckle was observed in OCI of living tissues caused by dynamic light scattering from the intracellular motions.⁴⁰ The dynamic speckle was used directly as an endogenous imaging contrast in MCI that could track the effects of antimitotic drugs on tissue health.²⁶ MCI captures the overall motion inside tissue, but is limited to imaging contrast.

In this paper, we extend MCI by incorporating fluctuation spectroscopy into holographic tissue dynamics spectroscopy (TDS). TDS is based on fluctuation spectrograms of living tissue responding to changing environments, internal metabolism, and xenobiotics. The basic operation of OCI and MCI are described in this section, followed by the algorithms to generate differential response spectrograms for TDS. All of the experimental work presented here uses multicellular tumor spheroids as the tissue model.

2.1 Multicellular Tumor Spheroids

Multicellular spheroids of normal cells or neoplastic cells (tumor spheroids) are balls of cells that may be easily cultured up to 1 mm in size *in vitro*.^{56,57} The spheroids can be used to simulate the optical properties of a variety of tissues,⁵⁸ such as the epidermis and various epithelial tissues, and may be used to simulate

the histological and metabolic features of small nodular tumors in the early avascular stages of growth.⁵⁷

Beyond a diameter of about 200 microns most spheroids develop a necrotic core surrounded by a shell of viable, proliferating cells, with a thickness varying from 100 to 300 μm . The limiting factor for necrosis development is oxygen—the oxygen consumption and oxygen transport reflecting the status of the spheroid.⁵⁹ Early work on spheroids⁶⁰ studied therapeutic strategies for cancer, especially the spheroid response to different drugs. The response to drug therapy was quantified from an analysis of spheroid volume growth delay, increase in the necrotic area, and change in survival capacity. This work focused on hypoxia and its induction by chemical agents.⁶¹ None of these studies considered cellular and sub-cellular motility as a diagnostic of cellular vitality, despite the obvious utility of this diagnostic, because there was no means of nondestructively detecting motility throughout a volume. Motility contrast imaging provides this capability up to a millimeter deep in tumor spheroids.

Tumor spheroids of permanent cell lines are a reliable model for systematic studies of tumor response to therapy.^{62,63} Although the *in vitro* environment is artificial, the biochemistry, metabolism, and cell signaling response of cells grown as 3D constructs closely simulates *in vivo* tissue^{64–66} and more accurately captures their pathophysiology and response to therapy.⁶⁷ For example, spheroids from epithelial ovarian cancer,⁶⁸ hepatocellular carcinoma⁶⁹ and colon cancer⁷⁰ had expression profiles more like those from tumor tissues. The three-dimensional environment of the spheroids also presents different pharmacokinetics than 2D monolayer culture and produce differences in cancer drug sensitivities between monolayers and the spheroids.⁷¹ Therefore, *in vitro* experiments are a surrogate for *in vivo* response and have been used to test cancer therapeutics such as metabolic and chemical gradients, hypoxia, cell-cell and cell-matrix contacts, and chemoresistance.^{61,72}

We performed an experiment to identify apoptotic versus necrotic cells and tissues in a small (300 micron) tumor spheroid. Laser scanning confocal microscopy, using the dyes YO-PRO-1 and propidium iodide, permitted us to visualize live, apoptotic, and dead cells in small $<300 \mu\text{m}$ spheroids using a Nikon A1R confocal microscope. We scanned into 100 microns of tissue at 1 micron intervals. The YO-PRO-1 dye is a nuclear green fluorophore that stains the nuclei of apoptotic cells. Propidium iodide is a vital red fluorophore that stains necrotic or dead cells that have compromised membranes. The experimental results are shown Fig. 1(a) in two-channel color and numerically thresholded in Fig. 1(b) to show the central region of apoptotic cells and tissues (blue) and necrotic or dead cells (red). The confocal depth is shown in Fig. 1(c), penetrating to the region containing many apoptotic cells and tissue between the proliferating shell and the necrotic core. The proliferating shell is composed of healthy cells that form a coherent tissue, while the core has many voids filled with extracellular debris and bounded by rafts of apoptotic or necrotic cells, shown in a SEM in Fig. 1(d). In the spectrogram analysis described in Sec. 2.5, dynamic scattering is separately averaged over the proliferating shell and the necrotic core. The apoptotic transition region is relatively thin (about 50 microns thick) and is not explicitly contained in either the shell or core averages.

Multicellular Tumor Spheroid Physiology

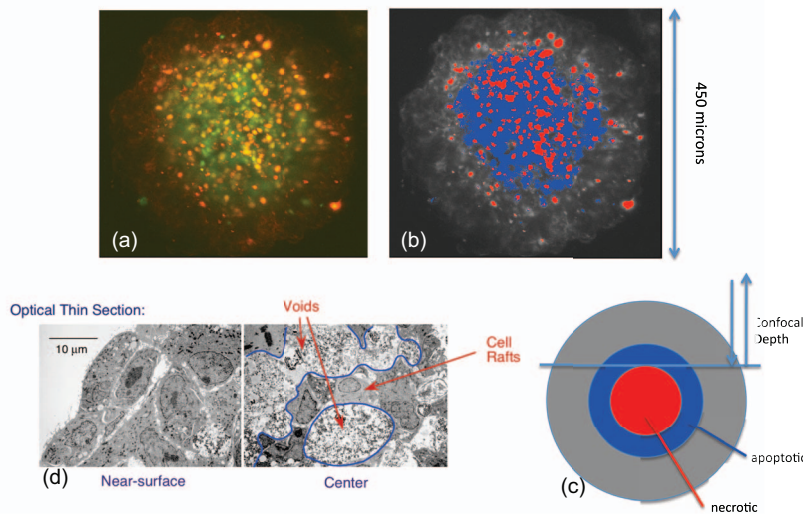


Fig. 1 Physiology of multicellular tumor spheroids. (a) The confocal image is a two-channel (green and red) image of apoptosis and necrosis. (b) The values are thresholded to show the apoptotic central region and necrotic cells. (c) The general structure of the spheroid with a proliferating shell surrounding a necrotic core and a transition region of apoptotic cells. (d) The spheroid has a shell of proliferating cells surrounding a core that contains voids of extracellular debris.

2.2 Holographic Optical Coherence Imaging

The basic optical system for holographic optical coherence imaging is shown in Fig. 2(a). We use a mode-locked Ti:sapphire laser (100 fs pulse duration, 100 MHz repetition rate) with a center wavelength of 840 nm and a bandwidth of 17 nm. The lenses L1 and L2 perform the Fourier transform of the object beam. The CCD camera is placed at the Fourier plane of the object, where the object beam interferes with the zero-path-matched reference beam that passes through the computer-controlled delay line. The typical object intensity for living tissue at the object plane is 5 mW/mm², and an 8-bit CCD camera with one mega-pixel resolution was used with an exposure time of 10 msec. Digital holograms were reconstructed by fast Fourier transform. An example of a pseudo-B-scan of a tumor spheroid is shown.

Holographic optical coherence imaging is based on off-axis digital holography using a CCD camera with a 7.4 micron pixel pitch. The nominal speckle size on the CCD chip is approximately nine pixels with approximately three optical fringes per speckle using a reference beam crossing angle of 3 deg at a wavelength of 840 nm. The intensity $I_H(x', y')$ is electronically captured by the CCD camera. A Fourier transform is used to reconstruct the digital hologram because the digital hologram is recorded at the Fourier plane. The Fourier transform of the intensity $I_H(x', y')$ is

$$\begin{aligned} FT(I_H) = & FT(|\psi_R|^2) + FT(|\psi_{OF}|^2) + FT(\psi_R * \psi_{OF}) \\ & + FT(\psi_R \psi_{OF}^*) \equiv F_1 + F_2 + F_3 + F_4, \end{aligned} \quad (1)$$

where the third term produces a holographic image, the fourth term produces a conjugate holographic image, and the first and second terms produce a zero-order image. The third and the fourth terms in Eq. (1) are

$$\begin{aligned} F_3(v_{x'}, v_{y'}) = & i\lambda f \psi_{R0} \exp\left(-\frac{i4\pi f}{\lambda}\right) \\ & \times \psi_O(-\lambda f v_{x'} + \lambda f v_{x0}, -\lambda f v_{y'} + \lambda f v_{y0}), \end{aligned} \quad (2)$$

$$\begin{aligned} F_4(v_{x'}, v_{y'}) = & -i\lambda f \psi_{R0} \exp\left(\frac{i4\pi f}{\lambda}\right) \\ & \times \psi_O^*(\lambda f v_{x'} + \lambda f v_{x0}, \lambda f v_{y'} + \lambda f v_{y0}). \end{aligned} \quad (3)$$

The holographic image F_3 is located at $(\lambda f v_{x0}, \lambda f v_{y0})$ and the conjugate image F_4 is located at $(-\lambda f v_{x0}, -\lambda f v_{y0})$, which are spatially separated from the zero-order image. The numerical Fourier transformation of the digital hologram acquired at the Fourier plane provides both amplitude and phase information of the multiply-scattered light from the coherence-gated object depth. The zero-order image is removed by averaging the in-

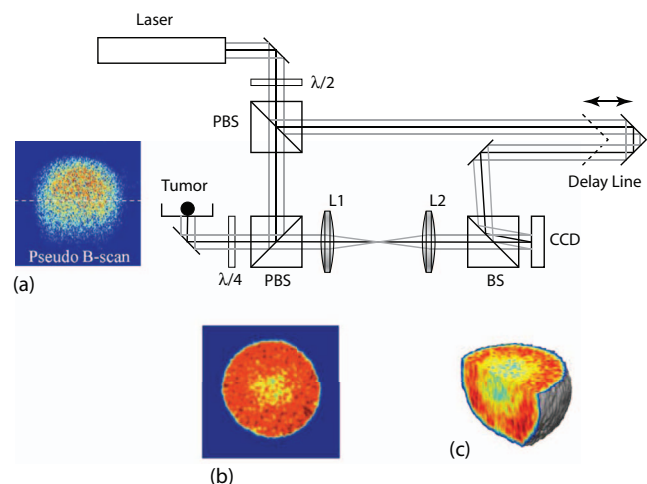


Fig. 2 (a) Experimental set-up. PBSs, polarizing beam splitters; BS, beam splitter; L1–L2, lenses; $\lambda/2$, half-wave plate; $\lambda/4$, quarter-wave plate. A pseudo B-scan showing reflectance in a vertical x-z section color coded on a log reflectance scale. (b) Motility contrast imaging from a horizontal x-y section, color-coded on a linear scale to intracellular motility. (c) Reconstructed volumetric motility image of a 800 micron-diameter tumor spheroid.

terference fringes over the fringe spacing interval. The fringe spacing for our crossing angle is approximately three pixels, and the digital hologram without interference is approximated by three-pixel averaging in the horizontal direction.

The resulting data format for holographic optical coherence imaging is a set of time-dependent two-dimensional intensity data $I(z; x, y; \tau, t)$ of the digitally reconstructed image at the coherence-gated depth z . The two time arguments τ and t correspond to the individual frames of a high frame-rate acquisition and to the long-term response of the tumor tissue, respectively. At a fixed depth, these data constitute a data cube of two spatial dimensions and one time dimension. For image representation in MCI, the normalized standard deviation (also known as temporal speckle contrast) is computed as

$$C(z; x, y; t) = \frac{\sqrt{\sum_{n=1}^N [I(z; x, y; \tau_n, t) - \bar{I}(z; x, y; t)]^2}}{\bar{I}(z; x, y; t)}, \quad (4)$$

where $\bar{I}(z; x, y; t) = \langle I(z; x, y; \tau_n, t) \rangle_n$ is the mean intensity for pixel (x, y) averaged along a series of N frames at a frame rate of $1/\Delta\tau$ acquired from the fixed depth z . This speckle contrast is represented through false color as a motility contrast image, for instance in Fig. 2(b). Red pixels denote high temporal fluctuations while blue pixels represent low temporal fluctuations. In the MCI example in Fig. 2(b), the proliferating shell surrounds the hypoxic and necrotic core of a tumor spheroid. A volumetric rendering of a tumor spheroid is shown in Fig. 2(c) color-coded with red highly active and yellow-green lower activity.

Motility contrast imaging provides a measure of the fluctuation magnitudes, but is not specific to fluctuations on different time scales, which are captured by fluctuation spectroscopy. The power spectra of the data are computed through the Fourier transform

$$\Phi(z; x, y; \omega, t) = \left| \frac{1}{\sqrt{2\pi}} \int_{-\infty}^{\infty} f(z; x, y; \tau, t) e^{-i\omega\tau} d\tau \right|^2 = \frac{F(z; x, y; \omega, t) F^*(z; x, y; \omega, t)}{2\pi}, \quad (5)$$

which gives an individual power spectrum for each pixel $(z; x, y)$ of the dataset. These individual pixel spectra are averaged over distinct portions of the tumors (for instance the shell or the core)

$$S_i(\omega, t) = \frac{\sum_{x, y \in i} \Phi(z; x, y; \omega, t)}{\left\langle \sum_{x, y \in i} \Phi(z; x, y; \omega, t) \right\rangle_\omega}, \quad (6)$$

where i = shell or core. The mean value of the power spectral density in the denominator is used to normalize each dataset to remove long-term laser intensity drift. The mean value is taken by integrating along the frequency axis, which is equivalent to normalizing by the integral in Parseval's Theorem. The spectral function $S_i(\omega, t)$ is a relative function that expresses the relative spectral contrast.

2.3 Autocorrelation Analysis and Multiple Scattering

For a dilute collection of scatterers, the single-scatter coherence-gated speckle intensity from a fixed depth and spatial location (x, y) on the reconstructed image plane has a temporal

autocorrelation^{31,73}

$$A_I(\tau) = \frac{\langle I(0)I(\tau) \rangle}{\bar{I}^2} = \exp[-q^2 \Delta z^2(\tau)], \quad (7)$$

where $q = 4\pi n_m/\lambda$ is the backscattering vector amplitude and $\Delta z^2(\tau)$ is the mean-squared displacement of the scattering objects. If the scattering objects are freely-diffusing, have homogeneous properties, and are dilute, then the mean-squared displacement is $\Delta z^2(\tau) = D\tau$, where D is the diffusion coefficient.

However, living tissue deviates in many important ways from the model of a dilute set of freely diffusing homogeneous particles. First, it is not dilute, but rather consists of a high density of scattering sites with multiple scattering and coherent light propagating up to 12 mean-free paths through the sample. Second, living tissue is highly heterogeneous in the size and density of scattering structures. Third, cells are highly active systems, with active transport inside the cell and active motions of the cell membrane, far from thermal equilibrium that precludes application of the equipartition theorem or the fluctuation dissipation theorem.^{4,11} Most of the assumptions that are at the basis of Eq. (7) are not valid under these conditions. In spite of this complexity of living tissue, the general phenomenology remains if the parameters are replaced by effective parameters that are related to the properties of the scattering sample.

2.3.1 Multiple scattering

Multicellular tumor spheroid tissue is an optically dense material with short scattering lengths (approximately 10 microns) but high anisotropy with $g = \langle \cos \theta \rangle \approx 0.9$ (Refs. 74 and 75) that causes most scattering to be in the forward direction and with transport lengths of approximately 100 microns. In a backscattering experimental configuration, the scattering is mostly forward scattering, up to a single backscatter event, and then the backscattered light is forward scattered back to the tissue surface.⁷⁶ The photon phase perturbations caused by dynamic scattering (moving scatterers) accumulate on each scattering event. Therefore, a coherence-gated photon from a fixed optical depth L in tissue has acquired $2L/l_s$ forward scattering random phase modulations and a single backscattering phase modulation

$$q_{eff}^2 \Delta z^2 = [2(L/l_s)q_F^2 + q_B^2]\Delta z^2. \quad (8)$$

The average forward scattering vector amplitude is $q_F^2 = 2k^2(1 - \langle \cos \theta \rangle) = 2k^2(1 - g)$, which is approximately 0.4 k , compared with $q_B = 2k$ for backscattering, which is a factor of 5 larger. Clearly, for small depths L relative to a mean free path, the backscattering dominates. The cross-over from single backscattered-dominated rates to multiple forward-scattered-dominated rates occurs at a coherence-gated depth L given by

$$L = \frac{l_s}{(1 - g)} = l_s^*. \quad (9)$$

This result is similar to those obtained by considering coherence-gated diffusion wave spectroscopy.^{38,39,77} For $g = 0.9$, the cross-over depth is about $L = 100$ microns. Our

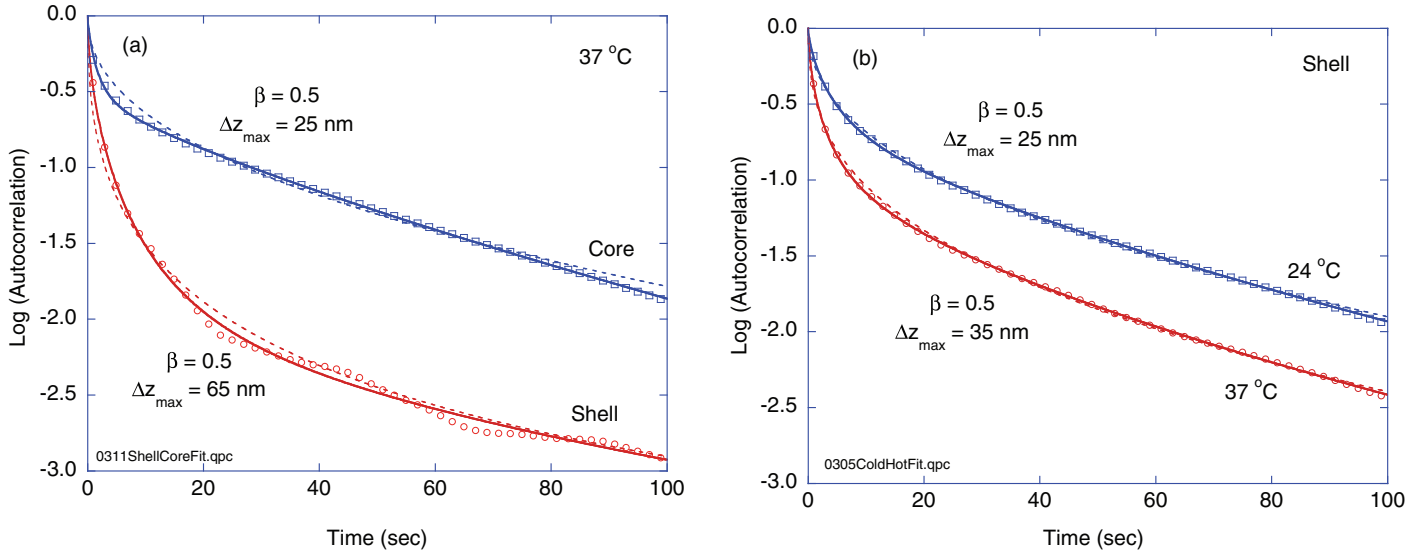


Fig. 3 Temporal autocorrelation functions of the holographically-gated intensity fluctuations from tumor spheroids. (a) Comparison of the shell and the core at 37°C. (b) Comparison of the shell at room temperature compared with physiological temperature. The solid curve is the two-component fit. The dashed curve is the constrained diffusion fit.

data are commonly obtained from between 200 to 400 microns inside the tumor spheroids. However, it is important to consider that autocorrelations are calculated over stochastic ensembles, and the autocorrelation function will not be a simple single exponential function of the argument in Eq. (8). There are many different scattering sources within cells and many different dynamical processes, and all of these mix and contribute to the scattered light. The main challenge of this ensemble spectroscopy is to separate out the different types of sub-cellular contributions to the multiple dynamic light scattering. This will be partially achieved using differential response spectrograms discussed later in this section.

2.3.2 Anomalous diffusion

The strong activity of living tissue makes many contributions to the mean-squared displacement Δz^2 , much of which is active motion of the cytoskeleton driven by molecular motors. However, few components of living tissue are free to move, but are usually constrained. For instance, diffusing particles can be confined within compartments,⁷⁸ and membrane undulations are limited by elastic harmonic potentials.^{79,80} The simplest extension of free diffusion is called anomalous diffusion^{81,82} with a mean-squared displacement time dependence given by

$$\Delta z^2(t) = D^* \left(\frac{t}{t_0} \right)^\beta. \quad (10)$$

If $\beta > 1$, the diffusion is called super-diffusion and if $\beta < 1$, the diffusion is called sub-diffusion. Both super-diffusion and sub-diffusion relate to correlations in the motion of scattering objects. Super-diffusion occurs when there is persistent motion of a particle, as for active transport of vesicles by molecular motors,⁸³ while sub-diffusion occurs if motion is constrained. Constrained diffusion occurs in a compartment or a harmonic potential, which has the time dependence

$$\Delta z^2(t) = \Delta z_{\max}^2 \{1 - \exp[-(\Gamma t)^\beta]\}, \quad (11)$$

where Δz_{\max}^2 is a maximum averaged value and Γ is a relaxation rate.

As an example, the autocorrelations of coherence-gated intensities from a fresh tumor spheroid are shown in Fig. 3(a) for the core of the tumor compared with the proliferating shell, and in Fig. 3(b) for the shell at room temperature compared with the shell at physiological temperature. Each of the autocorrelation data are fit both by the constrained diffusion model of Eq. (11) and by a two-component autocorrelation decay given by

$$A_I(\tau) = [A_1 e^{-(\tau/\tau_1)^\beta} + (1 - A_1) e^{-(\tau/\tau_2)^\beta}]^2. \quad (12)$$

Both fits are nearly equally good, with similar anomalous diffusion exponents of $\beta \approx 0.5$. Neither model is strictly correct, but each provides a different perspective on effective fluctuation properties of the tissue. In the case of the two-component decay, characteristic time constants are extracted, while in the case of the single constrained diffusion, a root-mean-squared maximum displacement may be estimated.

The constrained-diffusion model is used to estimate the maximum root-mean-squared displacement from the data in Fig. 3 that were obtained at a depth of approximately 1.5 mean transport lengths for three mean transport lengths double-pass. Accounting for this factor of three from multiple scattering, the maximum root-mean-squared displacement of shell and the core are $\Delta z_{\max} = 65$ and 25 nm , respectively. The fluctuation amplitudes of the tissue in the inactive core of the tumor spheroid are consistent with thermal membrane undulations, while the proliferating outer shell is much more active and far from equilibrium.^{84,85} Because of multiple scattering and the complexity of intra-tissue motions, these values must be viewed as effective values. However, these values can be compared to thermal undulation amplitudes of cell membranes that have values near 30 nm (Ref. 86) that are smaller than the values measured in the proliferating tissue, but are comparable with the values measured in the core. For the comparison between

room and physiological temperatures in Fig. 3(b), the maximum root-mean-squared displacement increases by 40%, even though the thermodynamic temperature rise alone for membrane undulations is expected to be only 2%. These interpretations are consistent with active and energetic processes of the cell dominating intracellular motions in the proliferating shell far from thermodynamic equilibrium.

The two-component model can be used to extract characteristic fluctuation times from the data in Fig. 3. In Fig. 3(a), the shell has two time constants $\tau_1 = 2$ s and $\tau_2 = 50$ s, while the core has $\tau_1 = 1.2$ s and $\tau_2 = 50$ s. The main difference in the behavior in this case is in the relative contributions, with the short-time component comprising a much larger fraction in the shell than in the core. Similarly, for the shell temperature effects, the room temperature values from the fits in Fig. 3(b) are $\tau_1 = 2.8$ s and $\tau_2 = 50$ s, while the physiological temperature data have $\tau_1 = 1.5$ s and $\tau_2 = 36$ s. These times lead to characteristic knee frequencies that appear in the power spectra discussed in Sec. 2.4.

2.4 Fluctuation Spectra

The autocorrelation functions are related to the spectral power densities through the Wiener-Khintchine theorem as

$$A_i(\tau, t) = FT^{-1}[S_i(\omega, t) - S_i(0, t)\delta(\omega)], \quad (13)$$

in which the DC frequency term is removed. This theorem places a one-to-one correspondence between autocorrelation functions and spectral power densities, and hence, they contain the same information about the fluctuating system. However, $A(\tau)$ and $S(\omega)$ provide complementary perspectives on the physics of the fluctuating system, often with different emphasis. For instance, eigenfrequencies or frequency bands in a dynamical system are more naturally expressed in the frequency domain, although biological samples are strongly damped systems that suppress oscillations.⁸⁷ In addition, very fast but low-amplitude phenomena tend to be more easily visualized in the frequency domain.

In the case of dynamic light scattering under heterodyne detection conditions, the power spectrum is

$$S(\omega) = FT\{\exp[-q_{eff}^2\Delta z^2(\tau)]\}. \quad (14)$$

When the mean-squared displacement takes on the form of Eqs. (10) and (11) for anomalous and constrained diffusion, the frequency dependence of the spectral power density can be approximately expressed as

$$S(\omega) \sim \frac{1}{1 + \left(\frac{\omega}{\omega^*(\beta')}\right)^{1+\beta'}}, \quad (15)$$

where $\omega^*(\beta')$ is a characteristic frequency that depends on the exponent β' that is closely related to, but not identical with, the anomalous diffusion exponent β . However, experimental spectral power densities usually show important deviations from Eq. (15), the most notable deviation being near the Nyquist sampling frequency. At this frequency, higher frequency motion can be “freeze-framed” or “strobed” by a fast sampling time (wide detection bandwidth) that is much shorter than the Nyquist period.⁸⁸

An example of a spectral power density is shown in Fig. 4(a) for the same data as in Fig. 3(a) for the shell and core of a fresh tumor spheroid. The shell data have a clear knee frequency around 0.1 Hz, followed by $1/f^{\beta'+1}$ behavior at a higher frequency with an exponent $\beta' \approx 0.4$. The necrotic core has a less distinct, but lower, knee frequency with a lower exponent $\beta' \approx 0.2$. Both spectra have similar noise floors at the Nyquist frequency of 5 Hz. The detection bandwidth for these data is $f_B = 16$ Hz, so part of the noise floor is caused by higher-frequency motions that are “freeze-framed” by the 10 msec acquisition speed of the camera. Motion in the living tissue up to 16 Hz is captured by the fast exposure, even though the frequencies are not resolved. The dependence of the noise floor on exposure time can provide an indication of the amount of high-frequency dynamics in the scattered light. The power spectra in Fig. 4(b) are for the shell at room and physiological temperatures. The characteristic frequencies shift higher for the warmer case, with a higher Nyquist floor reflecting higher frequency content between 5 and 16 Hz.

2.5 Fluctuation Differential Spectrograms

When perturbations are applied to a living tissue sample, the response of the tissue dynamics can be subtle, but consistent. Because both the autocorrelation and spectral density functions span a wide dynamic range over several orders of magnitude, small changes in dynamics are de-emphasized in logarithmic plots. To capture the time course of subtle changes in tissue dynamics requires a differential relative measure, which we take to be the differential relative spectrum

$$D(z; \omega, t) = \frac{S(z; \omega, t) - S(z; \omega, 0)}{S(z; \omega, 0)}. \quad (16)$$

This differential spectrogram is a two-dimensional function of frequency and time at fixed depth z , that captures the changes in the spectral power density as a function of time normalized by an appropriate spectral density, usually taken as the spectrum prior to the perturbation. The differential spectrogram shows positive and negative deviations from the nominal values across a wide frequency range.

An example of shell and core spectrograms for a tumor spheroid held in culture for 18 h are shown in Fig. 5. The spectral frequency is along the y -axis and spans three decades of dynamic range. Time is along the x -axis for this 18 h experiment. The baseline is set prior to $t = 0$ and is used as the quantity in the denominator of Eq. (16) for normalization. The change in the spectral content is plotted in false color, with deep red equal to 70% enhancement and deep blue equal to 70% inhibition. The response occurs in approximately three frequency bands that distinctly show different behaviors: low-frequency (0.005 to 0.1 Hz), mid-frequency (0.1 to 1 Hz), and high-frequency (1 to 5 Hz). The proliferating shell shows enhancements in the third frequency band after about an hour in medium, while the core shows nearly an opposite response. At low frequencies, the shell is mostly unchanged until a strong onset at about 18 h, while the core shows enhanced low frequencies for most of the duration of the experiment.

To interpret spectrograms, it is necessary to establish a correspondence of the frequencies observed in DLS with frequencies (and velocities and diffusion coefficients) obtained from the

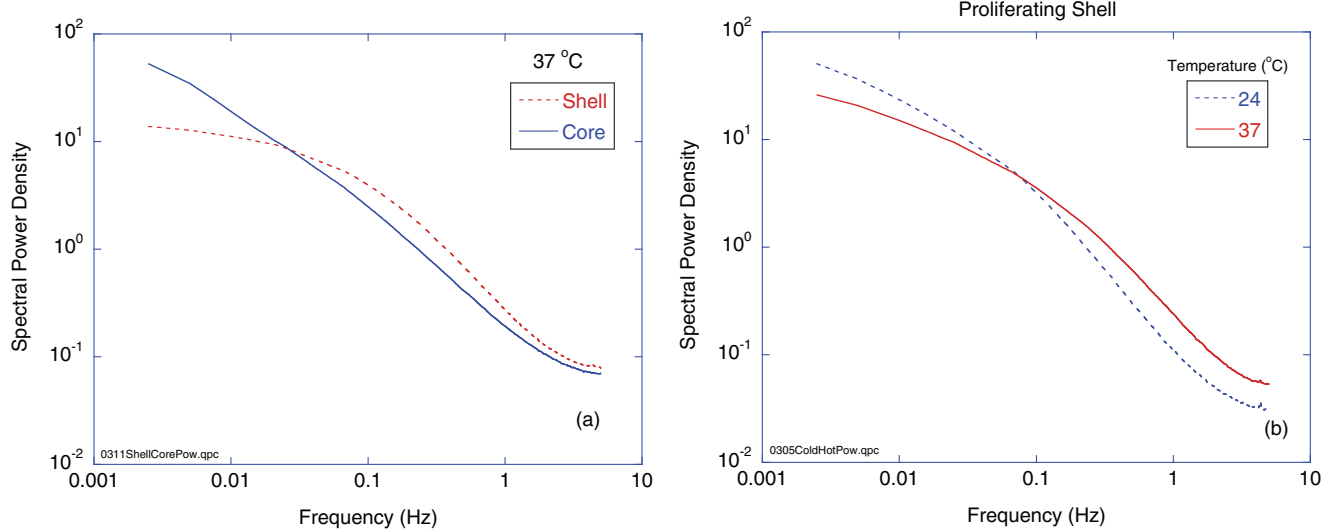


Fig. 4 Power spectra for the data of Fig. 3. (a) The power spectrum of the shell compared with the core at 37°C. (b) The power spectrum of the shell at 37°C compared with 24°C.

literature that are connected with specific biological targets and mechanisms. The lowest frequency in our experimental spectrograms is 0.005 Hz and the highest frequency is 5 Hz. We use the general relationships for single backscattering under heterodyne (holographic) detection: $q^2 D = \omega_D$ for diffusion and $qv = \omega_d$ for directed transport, where D is the diffusion coefficient and v is a directed speed. The smallest and largest frequencies that can be captured in the experiments define the physical ranges for directed transport and diffusion, respectively, which are $0.002 < v < 2 \mu\text{m/sec}$, and $8 \times 10^{-5} < D < 0.08 \mu\text{m}^2/\text{sec}$.

The velocity range is well within the range of intracellular motion in which molecular motors move organelles at speeds of microns per second.^{30,89–92} Diffusion of very small organelles, as well as molecular diffusion, are too fast to be resolved by

our maximum frame rate of 10 fps. Membrane undulations are a common feature of cellular motions, leading to the phenomenon of flicker.^{86,93–96} The characteristic frequency for membrane undulations tends to be in the range around 0.01 to 0.1 Hz.^{86,91,97} Results from the literature are summarized in Fig. 6. The graph is not exhaustive, and the size axis is only approximate. But the graph captures the general connection of spatial scale with temporal scale. Experiments on vesicles and the cytoplasm give the highest backscatter frequencies generally above 1 Hz and extending to tens of Hz. Larger mitochondria and organelles have slightly lower backscattering frequencies, but these are still in the range of band 3 frequencies of TDS. Membrane motions are much slower, coinciding with the frequencies of band 1 in TDS. This spatial-temporal trend is only semi-quantitative, but it provides a general principle that may help disentangle the

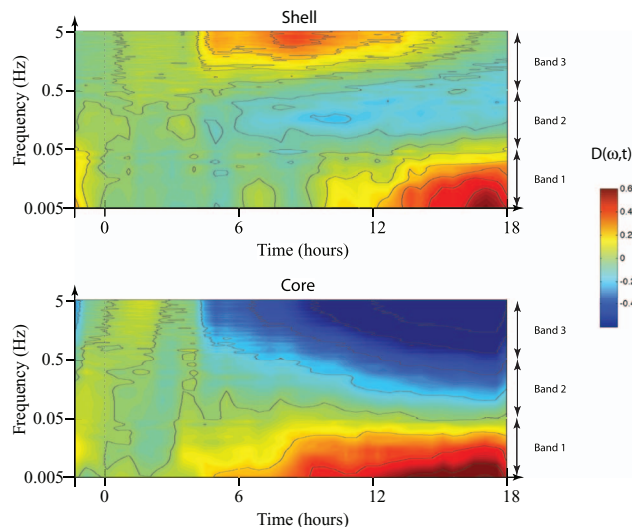


Fig. 5 Differential spectrograms for the proliferating shell and inner core. The frequency range is composed of roughly three bands that span three decades: band 1 from 0.005 to 0.05 Hz, band 2 from 0.05 to 0.5 Hz, and Band 3 from 0.5 Hz and higher.

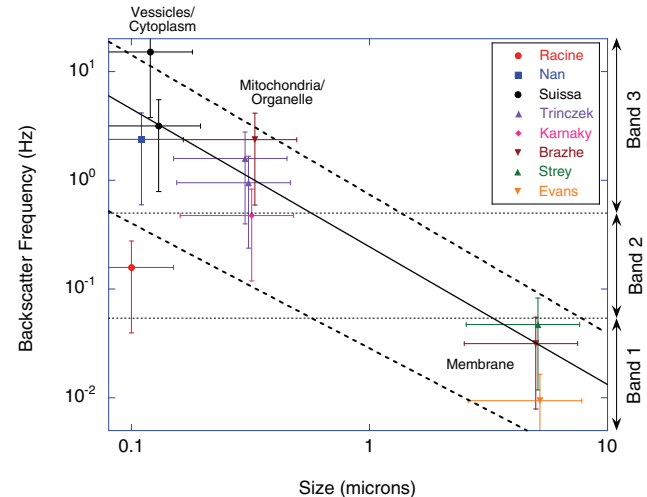


Fig. 6 QELS dynamic backscatter frequencies for $\lambda = 840$ nm calculated from mobility experiments in the literature from Refs. 30, 86, 89–92, and 97, and 98. The sizes are only approximate to show a general trend of lower frequencies for larger motions.

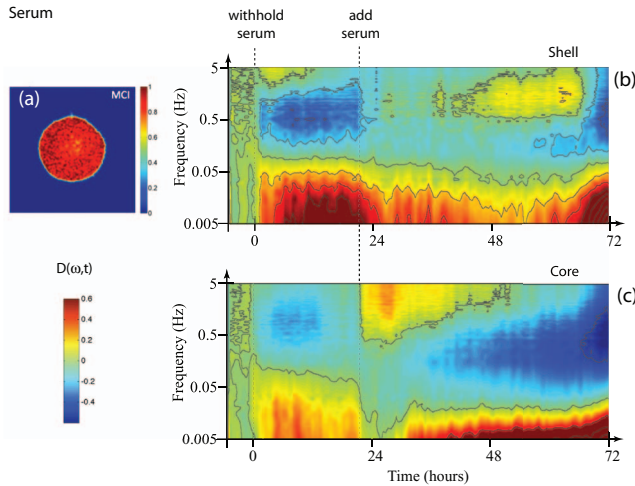


Fig. 7 Effect of serum in the growth medium. Serum in the growth medium was removed and then replaced after about 24 h. (a) The motility contrast image of the tumor. (b) The temporal speckle contrast versus time for the shell and (c) core. When serum is replenished after 24 h, the core shows immediate increased activity, but the shell shows a high-frequency response that was delayed about 24 h after the serum was reapplied.

mixtures of frequencies that arise from multiple dynamic light scattering mechanisms.

3 Tissue Preconditions

The proliferating and metabolic status of living tissue is complex and difficult to define precisely. Cells are constantly responding to their external and internal environments by changing their gene expression and molecular signaling. Therefore, it is important to consider the precondition of any tissue model prior to application of environmental or xenobiotic challenges and to recognize different initial conditions for a drug response study. The core of a small tumor (300 to 500 micron diameter) shows reduced motility, and is likely to be hypoxic, acidic, and ATP depleted. The response of tumors to drugs, or even to prolonged immobilization in a sample holder, depends on the initial condition. In particular, processes that require energy from ATP may not readily occur in the core, but would occur in the outer shell of the tumor spheroid.

Serum in the growth medium plays an important role in cell proliferation by providing essential growth factors that are required for cells to divide. The effect of removing serum and then reapplying it to a tumor is shown in Fig. 7. The motility contrast image of the mid-section of the tumor is in Fig. 7(a). The spectrograms for the shell and core are shown in Figs. 7(b) and 7(c), respectively. The baseline prior to $t = 0$ was taken with serum in the growth medium. New growth medium was applied at $t = 0$ without containing serum. Both the shell and the core show a shift in spectral weight to lower frequencies under this condition. At nearly 24 h, the growth medium with serum was restored. The replenished growth medium also has replenished oxygen and nutrients, which is a confounding factor preventing the formal isolation of the effect of serum. The core and shell show different responses to the restored serum. The core immediately responded with enhancement at high frequencies, likely because of the replenished oxygen and nutrients. Initially, the

shell response was not as dramatic. However, about 24 h after the serum was reapplied, there was an enhancement of high frequencies in the shell in the range around 3 Hz. It is possible that this is associated with mitosis of cells in the outer shell. The cell cycle of a collection of cells can be synchronized by removing and then reapplying growth factors, with a burst of cell division approximately 24 h (but with a broad range of times) after the growth factors are reapplied.

4 Environmental Perturbations

The tissue differential spectrograms are sensitive to subtle changes in the tissue environment and to internal cellular conditions. In this section, we survey the tissue response spectrograms for changing temperature (including heat shock), osmolarity, and medium pH.

4.1 Temperature and Heat Shock

The thermal experiment is shown in Fig. 8 over a course of 6 h. The temperature increased from 24 to 37°C, then up to 43°C (which is lethal to cells for long exposure times) and returned to physiological 37°C. The motility contrast image at the mid-section is shown in Fig. 8(a). Heating to physiological temperature from room temperature is accompanied by a large increase in the speckle contrast (temporal activity). The spectrograms of the outer shell and the core are shown in Figs. 8(b) and 8(c), respectively. The frequency range spans from 0.005 to 5 Hz. The baseline at 24°C is flat, then there is significant increase in the higher frequencies as the temperature rises to 37 and then to 43°C. Once at 43°C, the enhancement in high frequency motion begins to decay as the cells are stressed by the excessive heat. An important observation in this experiment is the behavior after the tissue is returned to the physiological 37°C temperature. The spectrogram shows clear differences post- to pre-heat-stress. In particular, there is an increase in the low frequencies at late times, which might be indicative of blebbing induced by heat shock. The proliferating shell shows a late strong high-frequency enhancement that is missing in the core. The high frequencies in the proliferating shell may be associated with apoptosis, while the hypoxic core undergoes necrosis in response to the heat shock. These data illustrate the differences that appear in the response spectrograms between the outer shell and the inner core, which are primarily distinguished by their initial metabolic activity and susceptibility to stress. If the high-frequency versus low-frequency differences between the shell and the core are caused by the differences between apoptosis and necrosis, then tissue dynamics spectroscopy would provide a fully endogenous way to probe this difference.

4.2 Osmolarity

Osmolarity has a strong effect on the uptake of water into cells and tissue. Hypotonic conditions lead to strong cellular swelling (edema) and possibly lysis, while hypertonic conditions desiccate the cells and cause them to contract. The refractive index of the cells decrease with swelling and produce less light scattering, which appears as a weaker backscattered signal. The overall brightness of the backscattered signal from the tumor spheroids is normalized out by our analysis and does not contribute to

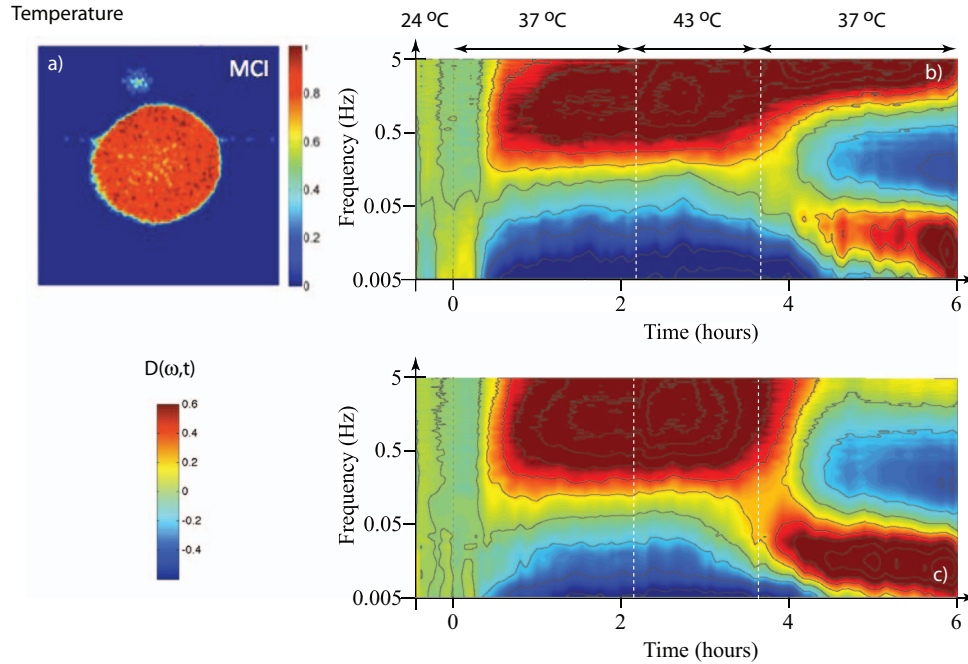


Fig. 8 Thermal response for an increase in temperature from 24°C to 37°C and then to 43°C. (a) Motility contrast image of a 400- μm diameter tumor; (b) and (c) differential spectral power densities for the shell and core, respectively.

the frequency changes in the differential relative spectrograms. We monitored the change in the relative spectral density as we changed the osmolarity of the growth medium at 24°C and at physiological temperature 37°C, as shown in Fig. 9.

At room temperature, the osmolarity was changed to 200 or 400 mOsm from isotonic conditions of 310 mOsm. The hypotonic condition caused an initial increase in high and mid frequencies, followed by a relaxation back to normal behavior. This transient effect is likely caused by the cell re-establishing homeostasis after the osmotic shock. For hypertonic conditions

with cell shrinkage, there is inhibition of the high frequencies and a significant increase in the low frequencies with no relaxation back to homeostasis. The suppression of high frequencies is associated with inhibited motions, possibly due to increased intracellular viscosity, while the enhanced low frequencies may be associated with cell shape changes as the cells desiccate.

At physiological temperature 37°C, the initial transients are similar to those at room temperature, but both the hypo- and hyper-tonic initial responses rapidly decay (within minutes) and are followed by a much stronger long-term behavior. For the

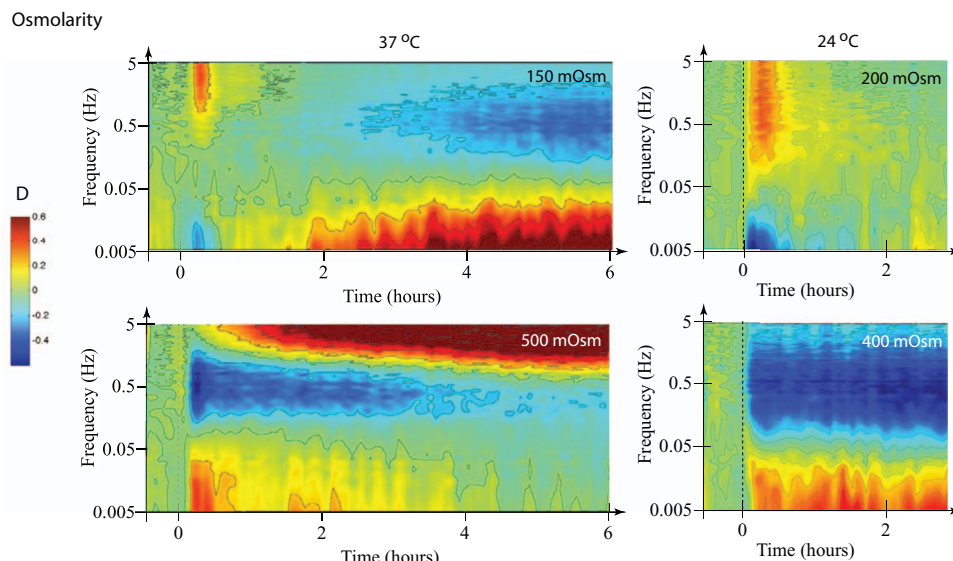


Fig. 9 Response of the relative spectral power to changes in osmolarity of the proliferating shell at 24°C and 37°C. The osmolarity is changed from isotonic (300 Osm) at $t = 0$. The hypotonic osmolarities of 200 and 150 mOsm induces swelling of the tumors. The hypertonic solutions of 400 and 500 mOsm cause tumor dessication and shrinkage.

long-term hypotonic condition (cell swelling), the low frequencies are significantly enhanced, while for the long-term hypertonic condition (cell shrinkage), the high frequencies are enhanced. The initial transient responses may be understood in terms of cell swelling and shrinking, which are similar to the room temperature response. Desiccation of the cytosol under hypertonic conditions shrinks the cell volume, increases the viscosity, and increases the density of intracellular constituents, significantly impeding motion. This is reflected in the initial increase of the low frequencies. The most dramatic difference between room and physiological temperatures is the high-frequency enhancement under cell desiccation at physiological temperature, which is absent at room temperature. Membrane vesicles would still be active as the cell tries to reestablish stasis, and might be associated with the high-frequency increase for the hypertonic condition at long times. Cell shrinkage is also associated with the loss of cell-cell contacts, and the high frequency content may be the rapid retraction of cell membrane after the contact is lost.

4.3 Response to pH

The pH of the growth medium is an important factor in tissue stasis. For instance, when CO₂ increases above 5% in the gas over the growth medium, this causes acidification of the growth medium and decreased viability of the cells and tissues. In addition, many solid tumors have acidic microenvironments, with the largest acidity in the center of the tumors (associated with the maximum hypoxia). Tumors responding to pH of 6 (acidic) and pH of 8 (basic) growth medium are shown in Fig. 10. The acidic conditions slow down the intracellular motions in both the shell and core, but with significantly more suppression in the core. This strong core response may be from the additive effects of the applied low pH to the naturally acidic core of the tumor spheroid. Conversely, the basic conditions enhance the higher frequencies in the shell of the tumor spheroid. There is a relatively mild response in the core, and no enhanced high frequencies, possibly because of the compensation of the internal acidity by the applied basic conditions.

5 Discussion

Holographic TDS, introduced in this paper, is a coherence-gated mode of DWS that captures differential spectrograms of tissue evolving under perturbations. Despite the complex nature of intracellular and cellular motions, the spectrograms capture a general scaling of size versus frequency, with low frequencies (0.005 to 0.1 Hz) related to gross cell shape changes, mid-frequencies (0.1 to 1 Hz) related to active membrane motions and high-frequencies (1 to 5 Hz) related to active organelle and vesicle motions. Because different types of environmental perturbations affect the cellular functions differently, the spectrograms become a kind of fingerprint of the specific perturbation.

In this paper, we do not make an explicit connection between TDS frequencies and biological mechanisms, but simply note that band 1 is consistent with membrane motions and band 3 is consistent with cytoplasm, vesicle, and organelle motions, as supported by a substantial body of work in the literature.^{30, 86, 89–92, 97, 98} The differential spectrograms represent a unique type of phenotypic profile. Phenotypic profiling is growing in utility for early drug discovery^{99, 100} because it uses physiological responses to help classify mechanisms of action. The differential spectrograms presented in this paper establish phenotypic profiles for environmental conditions that can be compared with future phenotypic profiles of response to drugs.

Although the choice of spectral representation of dynamic light scattering fluctuations contains no additional information compared with autocorrelation analysis, it does provide a more natural way to visualize subtle changes in fluctuations caused by mild perturbations. For instance, because differential spectrograms are normalized by the initial power spectrum, even small percent changes in high-frequency motions are captured with high contrast. This makes it possible to identify influences of the perturbations on relatively fast organelle and vesicle motions, even though these contribute only a small fraction to the overall fluctuations.

There are several open questions and challenges for holographic tissue dynamics spectroscopy. The chief questions relate

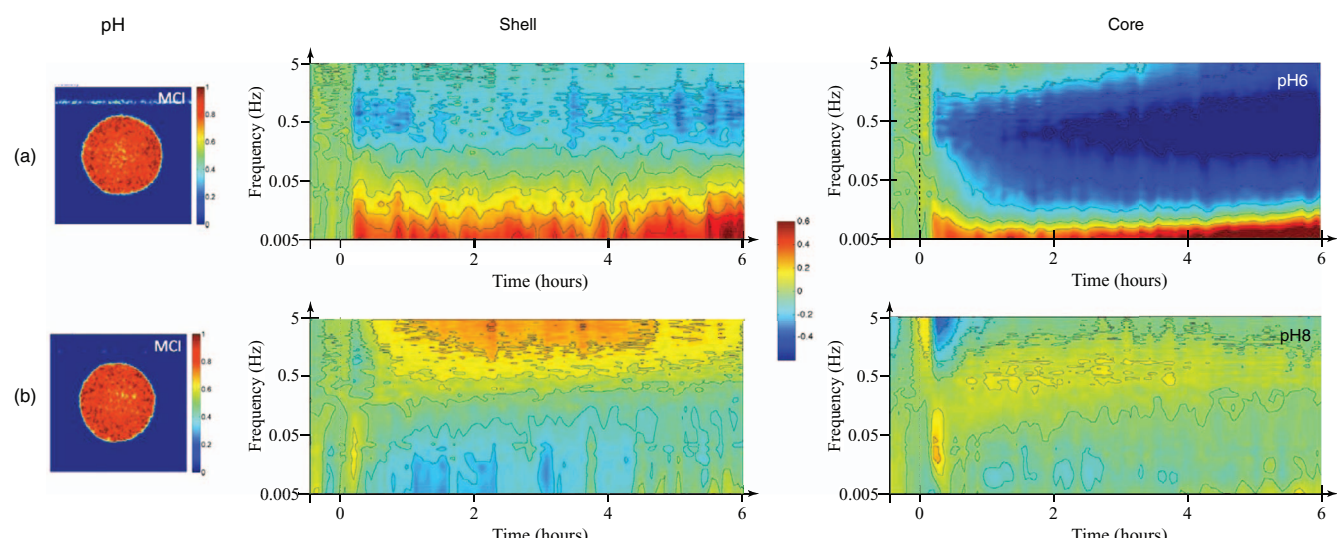


Fig. 10 Spectrogram fingerprints for response to (a) acidic (pH = 6) and (b) basic (pH = 8) conditions for proliferating shell and hypoxic core. The motility contrast images for the tumors are on the left.

to sensitivity and specificity of the technique, especially in future drug screening applications. The sensitivity of holography is a significant advantage, but carries the disadvantage of mechanical sensitivity to optical system vibrations. Common-path holography configurations could stabilize the optical system to allow broader laboratory use. In terms of specificity, different drugs or perturbations may have different modes of action, influencing different signaling pathways, but may share common physiological response. Because TDS probes the physiological rather than molecular response, it would not be able to distinguish these. On the other hand, the ability of TDS to track real-time dynamics already goes well beyond simple toxicity screens that rely on one-dimensional metrics, such as cell proliferation rate, as a single endpoint for a drug screen.

Acknowledgments

This work was supported by the National Science Foundation Grant No. CBET-0756005. Jeong gratefully acknowledges support from the Korea Military Academy Hwarangdae Research Institute.

References

1. A. Wax, C. H. Yang, V. Backman, K. Badizadegan, C. W. Boone, R. R. Dasari, and M. S. Feld, "Cellular organization and substructure measured using angle-resolved low-coherence interferometry," *Biophys. J.* **82**, 2256–2264 (2002).
2. A. W. C. Lau, B. D. Hoffman, A. Davies, J. C. Crocker, and T. C. Lubensky, "Microrheology, stress fluctuations, and active behavior of living cells," *Phys. Rev. Lett.* **91**, 198101 (2003).
3. T. D. Pollard, "The cytoskeleton, cellular motility and the reductionist agenda," *Nature* **422**, 741–745 (2003).
4. D. Mizuno, C. Tardin, C. F. Schmidt, and F. C. MacKintosh, "Nonequilibrium mechanics of active cytoskeletal networks," *Science* **315**, 370–373 (2007).
5. F. Julicher, A. Ajdari, and J. Prost, "Modeling molecular motors," *Rev. Mod. Phys.* **69**, 1269–1281 (1997).
6. C. P. Brangwynne, G. H. Koenderink, F. C. MacKintosh, and D. A. Weitz, "Intracellular transport by active diffusion," *Trends Cell Biol.* **19**, 423–427 (2009).
7. K. Luby-Phelps, "Cytoarchitecture and physical properties of cytoplasm: Volume, viscosity, diffusion, intracellular surface area," *Int. Rev. Cytol.* **192**, 189–221 (2000).
8. G. Massiera, K. M. Van Citters, P. L. Biancaniello, and J. C. Crocker, "Mechanics of single cells: Rheology, time dependence, and fluctuations," *Biophys. J.* **93**, 3703–3713 (2007).
9. T. M. Squires and T. G. Mason, "Fluid Mechanics of Microrheology," *Ann. Rev. Fluid Mech.* **42**, 413–438 (2010).
10. C. Wilhelm, "Out-of-equilibrium microrheology inside living cells," *Phys. Rev. Lett.* **101**, 028101 (2008).
11. F. Gallet, D. Arcizet, P. Bohec, and A. Richert, "Power spectrum of out-of-equilibrium forces in living cells: amplitude and frequency dependence," *Soft Matter* **5**, 2947–2953 (2009).
12. L. T. Perelman, "Optical diagnostic technology based on light scattering spectroscopy for early cancer detection," *Expert Review of Medical Devices* **3**, 787–803 (2006).
13. L. T. Perelman, V. Backman, M. Wallace, G. Zonios, R. Manoharan, A. Nusrat, S. Shields, M. Seiler, C. Lima, T. Hamano, I. Itzkan, J. Van Dam, J. M. Crawford, and M. S. Feld, "Observation of periodic fine structure in reflectance from biological tissue: a new technique for measuring nuclear size distribution," *Phys. Rev. Lett.* **80**, 627–630 (1998).
14. V. Backman, V. Gopal, M. Kalashnikov, K. Badizadegan, R. Gurjar, A. Wax, I. Georgakoudi, M. Mueller, C. W. Boone, R. R. Dasari, and M. S. Feld, "Measuring cellular structure at submicrometer scale with light scattering spectroscopy," *IEEE J. Sel. Top. Quantum Electron.* **7**, 887–893 (2001).
15. J. W. Pyhtila and A. Wax, "Polarization effects on scatterer sizing accuracy analyzed with frequency-domain angle-resolved low-coherence interferometry," *Appl. Opt.* **46**, 1735–1741 (2007).
16. K. J. Chalut, J. H. Ostrander, M. G. Giacomelli, and A. Wax, "Light scattering measurements of subcellular structure provide noninvasive early detection of chemotherapy-induced apoptosis," *Cancer Res.* **69**, 1199–1204 (2009).
17. Y. L. Kim, V. M. Turzhitsky, Y. Liu, H. K. Roy, R. K. Wali, H. Subramanian, P. Pradhan, and V. Backman, "Low-coherence enhanced backscattering: review of principles and applications for colon cancer screening," *J. Biomed. Opt.* **11**, 041125 (2006).
18. D. Huang, E. A. Swanson, C. P. Lin, J. S. Schuman, W. G. Stinson, W. Chang, M. R. Hee, T. Flotte, K. Gregory, C. A. Puliafito, and J. G. Fujimoto, "Optical coherence tomography," *Science* **254**, 1178–1181 (1991).
19. A. F. Fercher, W. Drexler, C. K. Hitzenberger, and T. Lasser, "Optical coherence tomography - principles and applications," *Rep. Prog. Phys.* **66**, 239–303 (2003).
20. S. C. W. Hyde, R. Jones, N. P. Barry, J. C. Dainty, P. M. W. French, K. M. Kwolek, D. D. Nolte, and M. R. Melloch, "Depth-resolved holography through turbid media using photorefraction," *IEEE J. Sel. Top. Quantum Electron.* **2**, 965–975 (1996).
21. M. Tziraki, R. Jones, P. M. W. French, M. R. Melloch, and D. D. Nolte, "Photorefractive holography for imaging through turbid media using low coherence light," *Appl. Phys. B: Lasers Opt.* **70**, 151–154 (2000).
22. P. Yu, M. Mustata, L. L. Peng, J. J. Turek, M. R. Melloch, P. M. W. French, and D. D. Nolte, "Holographic optical coherence imaging of rat osteogenic sarcoma tumor spheroids," *Appl. Opt.* **43**, 4862–4873 (2004).
23. K. Jeong, L. Peng, J. J. Turek, M. R. Melloch, and D. D. Nolte, "Fourier-domain holographic optical coherence imaging of tumor spheroids and mouse eye," *Appl. Opt.* **44**, 1798–1806 (2005).
24. E. Cuche, P. Marquet, and C. Depeursinge, "Simultaneous amplitude-contrast and quantitative phase-contrast microscopy by numerical reconstruction of Fresnel off-axis holograms," *Appl. Opt.* **38**, 6994–7001 (1999).
25. P. Marquet, B. Rappaz, P. J. Magistretti, E. Cuche, Y. Emery, T. Colomb, and C. Depeursinge, "Digital holographic microscopy: a noninvasive contrast imaging technique allowing quantitative visualization of living cells with subwavelength axial accuracy," *Opt. Lett.* **30**, 468–470 (2005).
26. K. Jeong, J. J. Turek, and D. D. Nolte, "Imaging motility contrast in digital holography of tissue response to cytoskeletal anti-cancer drugs," *Opt. Express* **15**, 14057–14064 (2007).
27. G. Maret and P. E. Wolf, "Multiple light-scattering from disordered media – the effect of brownian-motion of scatterers," *Z. Phys. B: Condens. Matter* **65**, 409–413 (1987).
28. D. J. Pine, D. A. Weitz, P. M. Chaikin, and E. Herbolzheimer, "Diffusing-wave spectroscopy," *Phys. Rev. Lett.* **60**, 1134–1137 (1988).
29. D. A. Boas and A. G. Yodh, "Spatially varying dynamical properties of turbid media probed with diffusing temporal light correlation," *J. Opt. Soc. Am. A Opt. Image Sci. Vis.* **14**, 192–215 (1997).
30. M. Suissa, C. Place, E. Goillot, and E. Freyssingea, "Internal dynamics of a living cell nucleus investigated by dynamic light scattering," *Eur. Phys. J. E* **26**, 435–448 (2008).
31. C. Joo, C. L. Evans, T. Stepinac, T. Hasan, and J. F. de Boer, "Diffusive and directional intracellular dynamics measured by field-based dynamic light scattering," *Opt. Express* **18**, 2858–2871 (2010).
32. S. H. Chen and F. R. Hallett, "Determination of motile behavior of prokaryotic and eukaryotic cells by quasi-elastic light-scattering," *Q. Rev. Biophys.* **15**, 131–222 (1982).
33. R. B. Tishler and F. D. Carlson, "A study of the dynamic properties of the human red-blood-cell membrane using quasi-elastic light-scattering spectroscopy," *Biophys. J.* **65**, 2586–2600 (1993).
34. A. Palmer, T. G. Mason, J. Y. Xu, S. C. Kuo, and D. Wirtz, "Diffusing wave spectroscopy microrheology of actin filament networks," *Biophys. J.* **76**, 1063–1071 (1999).
35. M. Heckmeier, S. E. Skipetrov, G. Maret, and R. Maynard, "Imaging of dynamic heterogeneities in multiple-scattering media," *J. Opt. Soc. Am. A Opt. Image Sci. Vis.* **14**, 185–191 (1997).

36. J. Li, G. Dietsche, D. Iftime, S. E. Skipetrov, G. Maret, T. Elbert, B. Rockstroh, and T. Gisler, "Noninvasive detection of functional brain activity with near-infrared diffusing-wave spectroscopy," *J. Biomed. Opt.* **10**, 044002 (2005).
37. D. A. Boas and A. K. Dunn, "Laser speckle contrast imaging in biomedical optics," *J. Biomed. Opt.* **15**, 011109 (2010).
38. A. Wax, C. H. Yang, R. R. Dasari, and M. S. Feld, "Path-length-resolved dynamic light scattering: modeling the transition from single to diffusive scattering," *Appl. Opt.* **40**, 4222–4227 (2001).
39. K. K. Bizheva, A. M. Siegel, and D. A. Boas, "Path-length-resolved dynamic light scattering in highly scattering random media: the transition to diffusing wave spectroscopy," *Phys. Rev. E* **58**, 7664–7667 (1998).
40. P. Yu, L. Peng, M. Mustata, J. J. Turek, M. R. Melloch, and D. D. Nolte, "Time-dependent speckle in holographic optical coherence imaging and the state of health of tumor tissue," *Opt. Lett.* **29**, 68–70 (2004).
41. D. A. Boas, K. K. Bizheva, and A. M. Siegel, "Using dynamic low-coherence interferometry to image Brownian motion within highly scattering media," *Opt. Lett.* **23**, 319–321 (1998).
42. A. L. Petoukhova, W. Steenbergen, T. G. van Leeuwen, and F. F. M. de Mul, "Effects of absorption on coherence domain path length resolved dynamic light scattering in the diffuse regime," *Appl. Phys. Lett.* **81**, 595–597 (2002).
43. B. Varghese, V. Rajan, T. G. Van Leeuwen, and W. Steenbergen, "Path-length-resolved measurements of multiple scattered photons in static and dynamic turbid media using phase-modulated low-coherence interferometry," *J. Biomed. Opt.* **12**, 024020 (2007).
44. K. Jeong, J. J. Turek, and D. D. Nolte, "Speckle fluctuation spectroscopy of intracellular motion in living tissue using coherence-domain digital holography," *J. Biomed. Opt.* **15**, 030514 (2010).
45. P. Yu, M. Mustata, P. M. W. French, J. J. Turek, M. R. Melloch, and D. D. Nolte, "Holographic optical coherence imaging of tumor spheroids," *Appl. Phys. Lett.* **83**, 575–577 (2003).
46. M. Laubscher, M. Ducros, B. Karamata, T. Lasser, and R. Salathe, "Video-rate three-dimensional optical coherence tomography," *Opt. Express* **10**, 429–435 (2002).
47. A. Dubois, K. Grieve, G. Moneron, R. Leaque, L. Vabre, and C. Boccaro, "Ultrahigh-resolution full-field optical coherence tomography," *Appl. Opt.* **43**, 2874–2883 (2004).
48. B. Karamata, M. Leutenegger, M. Laubscher, S. Bourquin, T. Lasser, and P. Lambelet, "Multiple scattering in optical coherence tomography. II. Experimental and theoretical investigation of cross talk in wide-field optical coherence tomography," *J. Opt. Soc. Am. A Opt. Image Sci. Vis.* **22**, 1380–1388 (2005).
49. S. C. W. Hyde, N. P. Barry, R. Jones, J. C. Dainty, and P. M. W. French, "Sub-100 micron depth-resolved holographic imaging through scattering media in the near-infrared," *Opt. Lett.* **20**, 2330–2332 (1995).
50. D. D. Nolte, "Semi-insulating semiconductor heterostructures: optoelectronic properties and applications," *J. Appl. Phys.* **85**, 6259–6289 (1999).
51. I. Yamaguchi and T. Zhang, "Phase-shifting digital holography," *Opt. Lett.* **22**, 1268–1270 (1997).
52. E. Cuche, F. Bevilacqua, and C. Depeursinge, "Digital holography for quantitative phase-contrast imaging," *Opt. Lett.* **24**, 291–293 (1999).
53. F. Dubois, L. Joannes, and J. C. Legros, "Improved three-dimensional imaging with a digital holography microscope with a source of partial spatial coherence," *Appl. Opt.* **38**, 7085–7094 (1999).
54. T. C. Poon, T. Yatagai, and W. Juptner, "Digital holography – coherent optics of the 21st century: introduction," *Appl. Opt.* **45**, 821 (2006).
55. K. Jeong, J. J. Turek, and D. D. Nolte, "Fourier-domain digital holographic optical coherence imaging of living tissue," *Appl. Opt.* **46**, 4999–5008 (2007).
56. P. Hargrave, P. W. Nicholson, D. T. Delpy, and M. Firbank, "Optical properties of multicellular tumour spheroids," *Phys. Med. Biol.* **41**, 1067–1072 (1996).
57. L. A. Kunz-Schughart, M. Kreutz, and R. Knuechel, "Multicellular spheroids: a three-dimensional in vitro culture system to study tumour biology," *Int. J. Exp. Pathol.* **79**, 1–23 (1998).
58. J. R. Mourant, T. M. Johnson, V. Doddi, and J. P. Freyer, "Angular dependent light scattering from multicellular spheroids," *J. Biomed. Opt.* **7**, 93–99 (2002).
59. K. Groebe and W. Mueller-Klieser, "On the relation between size of necrosis and diameter of tumor spheroids," *Int. J. Radiat. Oncol., Biol., Phys.* **34**, 395–401 (1996).
60. P. Freyer, P. L. Schor, K. A. Jarrett, M. Neeman, and L. O. Sillerud, "Cellular energetics measured by phosphorus nuclear-magnetic-resonance spectroscopy are not correlated with chronic nutrient deficiency in multicellular tumor spheroids," *Cancer Res.* **51**, 3831–3837 (1991).
61. W. Mueller-Klieser, "Three-dimensional cell cultures: from molecular mechanisms to clinical applications," *Am. J. Physiol.* **273**, 1109–1123 (1997).
62. L. A. Kunz-Schughart, "Multicellular tumor spheroids: intermediates between monolayer culture and in vivo tumor," *Cell Biol. Int.* **23**, 157–161 (1999).
63. G. Hamilton, "Multicellular spheroids as an in vitro tumor model," *Cancer Lett.* **131**, 29–34 (1998).
64. T. Jacks and R. A. Weinberg, "Taking the study of cancer cell survival to a new dimension," *Cell* **111**, 923–925 (2002).
65. A. Abbott, "Cell culture, biology's new dimension," *Nature* **424**, 870–872 (2003).
66. L. G. Griffith and M. A. Swartz, "Capturing complex 3D tissue physiology in vitro," *Nat. Rev. Mol. Cell Biol.* **7**, 211–224 (2006).
67. J. Friedrich, R. Ebner, and L. A. Kunz-Schughart, "Experimental anti-tumor therapy in 3-D: spheroids – old hat or new challenge?," *Int. J. Radiat. Biol.* **83**, 849–871 (2007).
68. N. A. L. Cody, M. Zietarska, A. Filali-Mouhim, D. M. Provencher, A. M. Mes-Masson, and P. N. Tonin, "Influence of monolayer, spheroid, and tumor growth conditions on chromosome 3 gene expression in tumorigenic epithelial ovarian cancer cell lines," *Biomed. Central Medical Genomics*, Vol. 1, Aug 7 2008.
69. T. T. Chang and M. Hughes-Fulford, "Monolayer and spheroid culture of human liver hepatocellular carcinoma cell line cells demonstrate distinct global gene expression patterns and functional phenotypes," *Tissue Eng. Part A* **15**, 559–567 (2009).
70. L. Gaedtke, L. Thoenes, C. Culmsee, B. Mayer, and E. Wagner, "Proteomic analysis reveals differences in protein expression in spheroid versus monolayer cultures of low-passage colon carcinoma cells," *J. Proteome Res.* **6**, 4111–4118 (2007).
71. I. Serebriiskii, R. Castello-Cros, A. Lamb, E. A. Golemis, and E. Cukierman, "Fibroblast-derived 3D matrix differentially regulates the growth and drug-responsiveness of human cancer cells," *Matrix Biol.* **27**, 573–585 (2008).
72. D. Khaitan, S. Chandra, M. B. Arya, and B. S. Dwarakanath, "Establishment and characterization of multicellular spheroids from a human glioma cell line; Implications for tumor therapy," *Journal of Translational Medicine* **4**, 12 (2006).
73. B. J. Berne and R. Pecora, *Dynamic Light Scattering: With Applications to Chemistry, Biology, and Physics*, Dover, New York (2000).
74. R. Richards-Kortum and E. Sevick-Muraca, "Quantitative optical spectroscopy for tissue diagnosis," *Ann. Rev. Phys. Chem.* **47**, 555–606 (1996).
75. J. R. Mourant, J. P. Freyer, A. H. Hielscher, A. A. Eick, D. Shen, and T. M. Johnson, "Mechanisms of light scattering from biological cells relevant to noninvasive optical-tissue diagnostics," *Appl. Opt.* **37**, 3586–3593 (1998).
76. D. A. Dewolf, "Electromagnetic reflection from an extended turbulent medium – cumulative forward-scatter single-backscatter approximation," *IEEE Trans. Antennas and Propag.* **AP19**, 254 (1971).
77. R. Carminati, R. Elaloui, and J. J. Greffet, "Beyond the diffusing-wave spectroscopy model for the temporal fluctuations of scattered light," *Phys. Rev. Lett.* **92**, 213903 (2004).
78. K. Ritchie, X. Y. Shan, J. Kondo, K. Iwasawa, T. Fujiwara, and A. Kusumi, "Detection of non-Brownian diffusion in the cell membrane in single molecule tracking," *Biophys. J.* **88**, 2266–2277 (2005).
79. R. Hirn, T. M. Bayer, J. O. Radler, and E. Sackmann, "Collective membrane motions of high and low amplitude, studied by dynamic light scattering and micro-interferometry," *Faraday Discuss.* **111**, 17–30 (1998).
80. J. O. Radler, T. J. Feder, H. H. Strey, and E. Sackmann, "Fluctuation analysis of tension-controlled undulation forces between giant vesicles and solid substrates," *Phys. Rev. E* **51**, 4526–4536 (1995).

81. R. Metzler and J. Klafter, "The random walk's guide to anomalous diffusion: a fractional dynamics approach," *Phys. Rep.* **339**, 1–77 (2000).
82. N. Gal and D. Weis, "Experimental evidence of strong anomalous diffusion in living cells," *Phys. Rev. E* **81**, 020903 (2010).
83. T. Soldati and M. Schliwa, "Powering membrane traffic in endocytosis and recycling," *Nat. Rev. Mol. Cell Biol.* **7**, 897–908 (2006).
84. L. C. L. Lin, N. Gov, and F. L. H. Brown, "Nonequilibrium membrane fluctuations driven by active proteins," *J. Chem. Phys.* **124**, 074903 (2006).
85. P. Bursac, B. Fabry, X. Trepaut, G. Lenormand, J. P. Butler, N. Wang, J. J. Fredberg, and S. S. An, "Cytoskeleton dynamics: fluctuations within the network," *Biochem. Biophys. Res. Commun.* **355**, 324–330 (2007).
86. H. Strey and M. Peterson, "Measurement of erythrocyte-membrane elasticity by flicker eigenmode decomposition," *Biophys. J.* **69**, 478–488 (1995).
87. E. M. Purcell, "Life at low reynolds-number," *Am. J. Phys.* **45**, 3–11 (1977).
88. A. B. Parthasarathy, W. J. Tom, A. Gopal, X. J. Zhang, and A. K. Dunn, "Robust flow measurement with multi-exposure speckle imaging," *Opt. Express* **16**, 1975–1989 (2008).
89. X. L. Nan, P. A. Sims, and X. S. Xie, "Organelle tracking in a living cell with microsecond time resolution and nanometer spatial precision," *ChemPhysChem* **9**, 707–712 (2008).
90. K. J. Karnaky, L. T. Garretson, and R. G. Oneil, "Video-enhanced microscopy of organelle movement in an intact epithelium," *J. Morphol.* **213**, 21–31 (1992).
91. N. A. Brazhe, A. R. Brazhe, A. N. Pavlov, L. A. Erokhova, A. I. Yusipovich, G. V. Maksimov, E. Mosekilde, and O. V. Sosnovtseva, "Unraveling cell processes: interference imaging interwoven with data analysis," *J. Biol. Phys.* **32**, 191–208 (2006).
92. B. Trinczek, A. Ebneth, and E. Mandelkow, "Tau regulates the attachment/detachment but not the speed of motors in microtubule-dependent transport of single vesicles and organelles," *J. Cell Sci.* **112**, 2355–2367 (1999).
93. F. Brochard and J. F. Lennon, "Frequency spectrum of flicker phenomenon in erythrocytes," *J. Phys. (Paris)* **36**, 1035–1047 (1975).
94. A. Zilker, M. Ziegler, and E. Sackmann, "Spectral-analysis of erythrocyte flickering in the 0.3-4-Mu-M-1 regime by microinterferometry combined with fast image-processing," *Phys. Rev. A* **46**, 7998–8002 (1992).
95. M. A. Peterson, H. Strey, and E. Sackmann, "Theoretical and phase-contrast microscopic eigenmode analysis of erythrocyte flicker – amplitudes," *J. Phys. II* **2**, 1273–1285 (1992).
96. Y. Z. Yoon, H. Hong, A. Brown, D. C. Kim, D. J. Kang, V. L. Lew, and P. Cicuta, "Flickering analysis of erythrocyte mechanical properties: dependence on oxygenation level, cell shape, and hydration level," *Biophys. J.* **97**, 1606–1615 (2009).
97. J. Evans, W. Gratzer, N. Mohandas, K. Parker, and J. Sleep, "Fluctuations of the red blood cell membrane: relation to mechanical properties and lack of ATP dependence," *Biophys. J.* **94**, 4134–4144 (2008).
98. V. Racine, M. Sachse, J. Salamero, V. Fraisier, A. Trбуil, and J. B. Sibarita, "Visualization and quantification of vesicle trafficking on a three-dimensional cytoskeleton network in living cells," *J. Microsc.* **225**, 214–228 (2007).
99. Y. Feng, T. J. Mitchison, A. Bender, D. W. Young, and J. A. Tallarico, "Multi-parameter phenotypic profiling: using cellular effects to characterize small-molecule compounds," *Nat. Rev. Drug Discovery* **8**, 567–578 (2009).
100. P. D. Caie, R. E. Walls, A. Ingleston-Orme, S. Daya, T. Houslay, R. Eagle, M. E. Roberts, and N. O. Carragher, "High-content phenotypic profiling of drug response signatures across distinct cancer cells," *Molecular Cancer Therapeutics* **9**, 1913–1926 (2010).